Quantum sensing using multiqubit quantum systems and the Pauli polytope

Irma Avdic,[1] LeeAnn M. Sager-Smith,[2] Indranil Ghosh,[1] Olivia C. Wedig,[1] Jacob S. Higgins,[1] Gregory S. Engel,[1] and David A. Mazziotti[1,*]

[1]*Department of Chemistry and The James Franck Institute, The University of Chicago, Chicago, Illinois 60637, USA*

[2]*Department of Chemistry and Physics, Saint Mary's College, Notre Dame, IN 46556, USA*

(Received 6 May 2023; accepted 14 September 2023; published 30 October 2023)

Quantum sensing has highly practical potential applications in fields ranging from fundamental physics and quantum communication to biophysics and bioengineering. However, achieving high fidelity and control of entangled qubits that enables sensing beyond the quantum limit is still a challenging endeavor. In this paper, we present an alternative approach to quantum sensing, which we call open-system quantum sensing, where we exploit a generalization of the Pauli exclusion principle to sense the openness of a multiqubit quantum system from only measurement of the qubit occupations. Qubit occupations of a pure state obey generalized Pauli exclusion constraints that define a convex set known as the Pauli polytope, and hence violation of one of these constraints—a facet of the polytope—reveals a mixed state from the interaction of a quantum system with its environment without performing full-state tomography. We examine experimental ultrafast spectroscopic data from the photosynthetic light-harvesting complex in green sulfur bacteria and show that we can sense and decode the relaxation of the complex due to environmental noise. More generally, we can apply open-system quantum sensing with any general multiqubit quantum system, where it provides a unique, visual approach that promises enhanced sensitivity and fidelity.

DOI: 10.1103/PhysRevResearch.5.043097

I. INTRODUCTION

Quantum sensors harness the high sensitivity of quantum systems to external disturbances to gain more information about the world around us. For example, technological applications of quantum sensing are found in precision timekeeping [1,2], high-energy physics [3], diagnostic screenings, and single-molecule detection [4–9]. Diamond-based spin qubits, in particular, present a promising platform for high-sensitivity measurements [10]. Optical and magnetic properties of spin defects are studied extensively, providing detailed information on their energy level structures, coherence times, and spin properties [11–16]. Sensing with a single electron spin, such as that in a negatively charged nitrogen-vacancy (NV) center in diamond, relies on optimization of the two-level spin dynamics. The NV center spin state can be readily initialized via optical pumps, coherently manipulated using pulsed radiation, and measured with high fidelity. A greatly desired scientific goal has been realizing entangled networks of such spin qubits, which allow for sensitivity measurements that surpass the standard quantum limit. Though significant experimental progress in ensemble sensing has been made [4,17–29], noise still presents a limitation in achieving greater coherence times of correlated sensors. To benefit from entanglement, it is necessary to understand the environmental fluctuations affecting the dynamics of the system of interest and the effect of internal degrees of freedom on the attainable sensitivity levels.

Fermionic systems naturally exhibit entanglement with a canonical example of a pair of indistinguishable fermions in an antisymmetric pure state [30,31]. In 1925, Pauli recorded that no more than one fermion can occupy a spin orbital [32], requiring the occupations of that orbital to be between zero and one. Additional restrictions on three-electron systems, known as the *generalized Pauli constraints* (GPCs), were discovered by Borland and Dennis in 1972, paving the way for the development of entanglement polytopes [33], GPC-based electronic structure algorithms [34–40], studies on fundamental symmetries of systems [41–45], and even experimental demonstrations of the phenomenon on quantum devices [46,47]. The advantage of considering GPCs in terms of quantum sensing becomes apparent when going beyond the 1-qubit sensing regime since the condition holds for p qubits, where p is arbitrary [40,48–50]. In this paper we present a scheme for open-system quantum sensing using a multiqubit quantum system. We provide a theoretical framework in terms of the set of one-particle reduced density matrices (1-RDMs) for sensing the openness of a 3-qubit system. The 1-RDM is defined by the integration of the N-fermion density matrix over the coordinates of all fermions except one:

$$^1D(1;\bar{1}) = \int {}^ND(12\cdots N;\bar{1}2\cdots N)d2d3\cdots dN. \quad (1)$$

The eigenfunctions of the 1-RDM are known as the natural orbitals ϕ_i, and the eigenvalues are natural-orbital occupation numbers n_i. By applying our model to the data available

*damazz@uchicago.edu

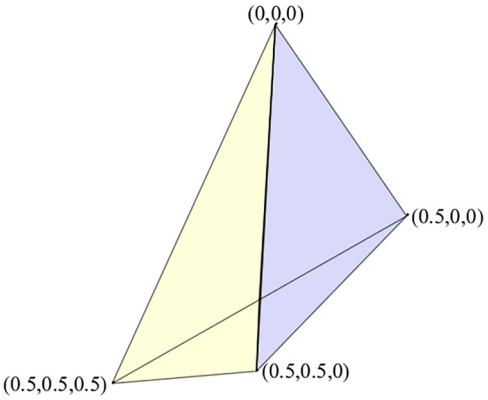

FIG. 1. A convex set formed from the ordered natural occupations of the 1-RDM for three fermions in six orbitals. The sets of occupations lying inside the yellow region of the polytope, the pure-state Pauli polytope, are compatible with at least one closed (pure-state) quantum system. Sets of natural occupations that lie in the blue region of the polytope are only compatible with an open (ensemble) quantum system.

from an experimental study of the eight-chromophore Fenna-Matthews-Olson (FMO) complex [51,52], we provide a practical analysis of a complex many-body environment and characterize the multiqubit sensing ability under realistic conditions. We extract the desired sensing information on the noise-assisted relaxation process in the system by examining multiple 3-qubit subsystems and their geometric 1-RDM-based pictures in the Pauli polytope (Fig. 1).

II. RESULTS

When the Pauli exclusion principle,

$$0 \leqslant n_i \leqslant 1, \tag{2}$$

is applied to the occupations of natural orbitals of the 1-RDM, n_i, it provides necessary and sufficient constraints that the 1-RDM is representable by at least one ensemble N-electron density matrix, also known as *ensemble N-representability conditions* [53]. In the presence of a third spin-$\frac{1}{2}$ particle, the *generalized Pauli constraints* (GPCs) for three fermions in six orbitals feature

$$n_5 + n_6 - n_4 \geqslant 0, \tag{3}$$

$$n_1 + n_6 = 1, \quad n_2 + n_5 = 1, \quad n_3 + n_4 = 1, \tag{4}$$

where $n_i \geqslant n_{i+1}$. They are also known as the *pure N-representability conditions* [48] since they only hold for pure states of three fermions. The sum rule for natural-orbital occupations in Eq. (4) is obeyed for all times, restricting the sum of the fermion population on each site to 1; therefore the system of three fermions in six orbitals can be treated as a system of 3 qubits [49]. In the case where fermions are also qubits, the GPCs for N fermions in $2N$ orbitals reduce to a single inequality [39,40,49] defined as

$$\sum_{i=N+2}^{r} n_i - n_{N+1} \geqslant 0, \tag{5}$$

where n_i are the smallest N eigenvalues for the system and r is the number of orbitals. Already for 3-qubit states there exist two physically distinct ways of entanglement represented by the Greenberger-Horne-Zeilinger $|\mathrm{GHZ}\rangle$ [54] and $|W\rangle$ [55] states. The ordered set of the three smallest 1-RDM eigenvalues of a 3-qubit system forms a polytope, a closed convex set with flat facets shown in Fig. 1. The polytope serves as a visual tool for the detection of entanglement between particles, i.e., the deviation of points from the (0,0,0) point in the polytope, which is the Slater determinant. Both the yellow and blue regions of the polytope are allowed for occupation numbers from an ensemble (open) system, but only the yellow region of the polytope is allowed for a pure-state system. We refer to this part as the pure-state Pauli polytope.

To apply the GPCs to entanglement-enhanced sensing, we consider a sample of the eight-exciton FMO complex, previously studied by Higgins *et al.* [52] in view of photosynthetic light harvesting, in particular, the variable steering of exciton energy transfer in reducing and oxidizing conditions. The FMO complex [51] is a well-characterized light-harvesting system present in green sulfur bacteria. It is composed of three monomers, each containing eight bacteriochlorophyll-a (BChla) chromophores (sites), which serve as a molecular wire that facilitates energy transfer from the light-harvesting antennae to the reaction center. The Hamiltonian for this system is described as

$$\hat{H} = \sum_{j=1}^{8} \hbar\omega_j \sigma_j^+ \sigma_j^- + \sum_{j \neq l} \hbar\nu_{j,l} (\sigma_j^- \sigma_l^+ + \sigma_j^+ \sigma_l^-), \tag{6}$$

where $\hbar\omega_j$ is the site energy of each chromophore, $\hbar\nu_{j,l}$ is the coupling constant between the pair of chromophores j and l, and σ_j^+ (σ_j^-) creates (annihilates) a single excitation on chromophore j. In natural conditions, many light-harvesting complexes contain at most one excitation at a given time [56]; therefore the representation of this system's density matrix can be restricted to an M-dimensional space of single excitations, where M is the number of chromophore sites [44]. Each of the eight chromophores is generally treated as a single α-spin fermion in a two-state model, where the two energy levels are separated by the excitation energy of the chromophore; so the terms *chromophore* and *qubit* are used interchangeably throughout this paper.

The FMO complex is extensively used as a platform for studying quantum phenomena [57–62] and, more recently, for machine learning and quantum information approaches to simulating energy transport processes in light-harvesting complexes [63–67]. This highly correlated exciton network features relaxation time on a timescale of femtoseconds and presents an ideal architecture for exploring the effects of entanglement on physical observables of interest in quantum sensing. Figure 2 shows the site population in the FMO complex for the first 1 ps of the energy transfer process at 77 K. We employ the 8×8 Hamiltonian given in Ref. [68] and an eight-exciton density matrix, D, that was initialized following an optical excitation as employed in the ultrafast spectroscopy experiments described in Ref. [52] (see Appendix B). The population dynamics are generated by evolving the Lindblad

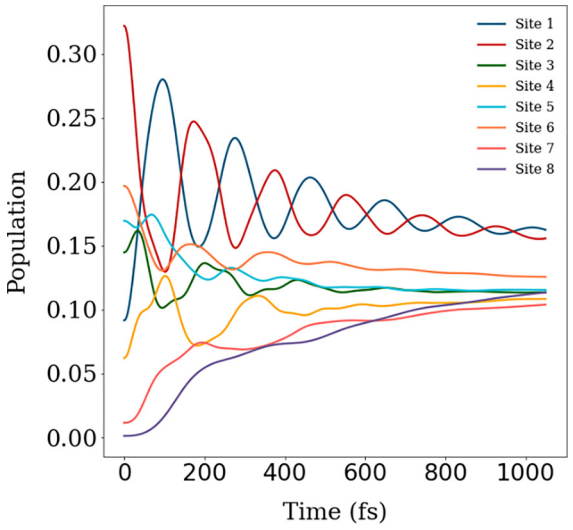

FIG. 2. Population dynamics of the FMO energy transfer process at 77 K in the site basis. The initial excitation oscillates among the eight sites but loses some of its population to environmental noise after 1 ps of the chromophore coherence lifetime.

equation,

$$\frac{d}{dt}D = -\frac{i}{\hbar}[\hat{H}, D] + \hat{L}(D), \tag{7}$$

where $\hat{L}$ is the Lindblad operator taken to be the sum of operators describing dephasing and dissipation of the system following the initial excitation [69]. The use of experimental values for dephasing and dissipation parameters, consistent with definitions in Ref. [70], along with the experimentally derived density matrix, provides a realistic treatment of the chromophore entanglement and its influence on the population dynamics. The initial excitation oscillates among the eight sites, after which the system relaxes and loses some of its initial population to dissipation into the environment. The experimental FMO sample was not attached to a reaction center; so the population loss is primarily due to quantum noise experienced by the system from its interaction with the environment.

The generalized Pauli constraints [Eq. (3)] allow us to model the relaxation process in the FMO complex by calculating the three smallest natural-orbital occupation numbers of the 3-qubit 1-RDMs obtained from the time evolution of the initial density matrix. The features of environmental noise and internal degrees of freedom on the time evolution trajectories are then inferred from the Pauli polytope. Figure 3 shows the trajectories of the natural occupation numbers of a 3-qubit FMO subsystem for 2 ps. The points colored black (red) show the spectrum outside (inside) the set of allowed 1-RDMs for pure quantum states. The FMO system is exposed to dephasing and dissipation noise; therefore the initial 1-RDM is ensemble N-representable, sharply violating the GPCs. The system then enters the pure set periodically and eventually converges to a classical ensemble, $(\frac{1}{8}, \frac{1}{8}, \frac{1}{8})$, where the excitation is spread equally among the eight sites. The equidistribution of energy over the degrees of freedom follows from the excitation reaching the classical limit over a

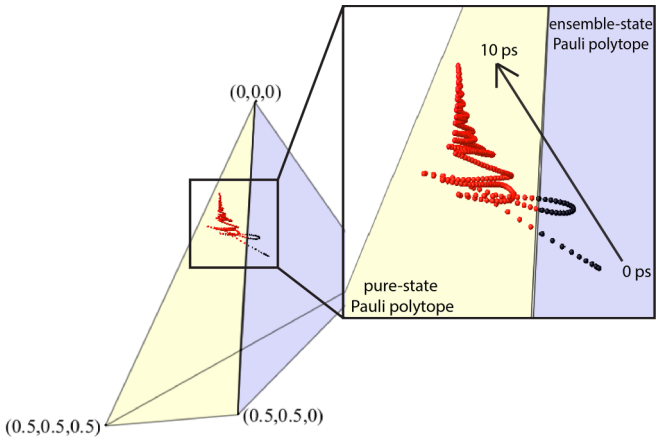

FIG. 3. Pauli polytope showing the femtosecond trajectories of a 3-qubit subsystem (chromophores 1, 2, and 3) from the experimentally derived density matrix of the FMO complex. The blue (yellow) region of the polytope shows the spectrum outside (inside) the set of allowed N-electron pure states, also denoted using black (red) spheres. Due to the presence of dephasing and dissipation, the spectrum of this open quantum system originates in the blue region of the polytope, violating the GPCs, and converges to a classical ensemble, in the yellow region, at 10 ps, obeying the GPCs for the most part of the temporal evolution.

sufficiently long period of time. In this scenario, the quantum noise, i.e., the environment, can be thought of as a quantum probe performing an indirect measurement on the 3 qubits in the system. Therefore, using the GPC framework, we are able to obtain geometric information about the openness of the 3-qubit system, i.e., its interaction with the environment, as a function of time from only a knowledge of its time-evolving 1-RDM. By measuring the temporal evolution of the openness of the system, we are able to sense the temporal evolution of the environment, providing us with an open-system quantum sensor. The use of a 3-qubit system is important because 3 is the smallest number of qubits whose 1-RDM can distinguish between an open (ensemble) and a closed (pure-state) quantum system [44]. Furthermore, the presence of 3 qubits supports an entangled multiparticle interaction that cannot be simulated by being broken into two-particle subsystems [33]. Our open-system quantum sensing approach can be represented using a generic quantum circuit model shown in Fig. 4. All 3 qubits are initially in the $|0\rangle$ state, which is flipped to $|1\rangle$ upon the excitation, as demonstrated with single-qubit

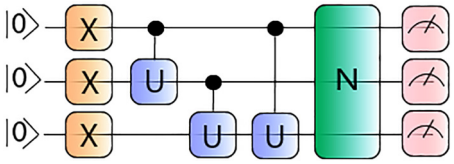

FIG. 4. Arbitrary quantum circuit model representing the open-system quantum sensing scheme for 3 qubits. The X and U gates function as traditionally ascribed, and the N gate represents environmental noise. The circuit is generic and does not illustrate a lower bound of the unitary gates needed to prepare an entangled 3-qubit state.

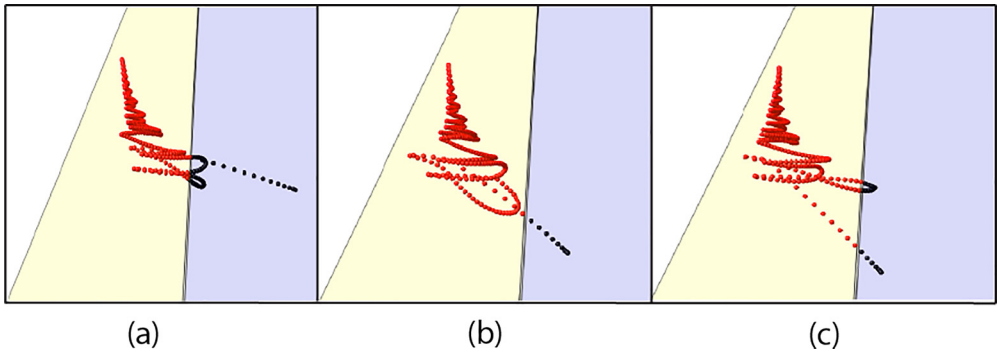

FIG. 5. Temporal trajectories of different 3-qubit subsystems of the FMO complex for the first 2 ps of the energy transfer process from the experimentally derived density matrix. In each case, the time evolution produces an expanded set of 1-RDMs, violating the GPCs initially, and then converges to the classical limit at longer times. The three panels differ in the choice of one of the 3 qubits or chromophores in the subsystem: (a) 124, (b) 125, and (c) 126, where, for example, "124" denotes chromophores 1, 2, and 4. Varying only 1 qubit shows enhanced measurements of the relaxation processes of the remaining qubits in the system.

X gates. Following this excitation, the qubits can be manipulated via unitary operations to prepare different entangled states. Finally, the noise operator, N, is applied, representing the environment interacting with the 3-qubit system. In this example, N may function as a well-defined Kraus operator that can be converted to unitary matrices in a dilation-based algorithm [64,71]. The measurements provide single-qubit populations used for decoding the relaxation process of this multiqubit system. If the prepared state is interacting with the environment, the pure-state Pauli polytope will be violated, demonstrating how the Pauli polytope can be used as a valuable tool for visualizing a quantum sensing process. The presented scheme provides a look at a general approach for embedding quantum computing and quantum sensing into a single platform for exploring ensemble and high-fidelity sensing regimes. Since the experimental data on the FMO complex only include information on dephasing and dissipation in the system, the theory focuses on those sources of quantum noise, which are also of significance as idle qubit errors in quantum information science. The advantage of embedding few-qubit quantum "computers" within quantum sensors is that we can exploit additional state preparations, measurements, and pure-state requirements, such as the GPCs or more general N-representability conditions, to enhance the sensitivity and fidelity of the sensors and improve postmeasurement analysis. Additionally, since we are considering a multiqubit system, this allows for conducting entangling measurements across multiple quantum states, a process polynomial in n, where n is the number of qubits, as opposed to measuring one state at a time.

To demonstrate the application of GPCs in quantum sensing, we highlight system-specific detection of the multiqubit relaxation process. Figures 5(a)–5(c) demonstrate spatially distinct trajectories exhibiting differences only based on the selection of the three chromophores in the 3-qubit subsystem: 124 [Fig. 5(a)], 125 [Fig. 5(b)], and 126 [Fig. 5(c)], where, for example, "124" denotes chromophores 1, 2, and 4. We observe that, in each system, the degrees of freedom of a single qubit enhance the measurement of the relaxation process of 2 correlated qubits. This demonstration establishes a relationship between entanglement, coherence time, and the generalized Pauli constraints. The violation of the GPCs certifies the openness of the quantum system, while the unique time evolution of the natural-orbital occupations, defining the GPCs and polytope, provides detailed information about the environment. This information can be mined visually, or by machine learning, to identify, assess, and understand variations that reflect (or sense) major or even nuanced changes in the environment. Such an open-system quantum sensor is able to enhance the measurement of energy relaxation processes by examining the effect of noise on the purity of the quantum state via the GPCs that define the facets of the pure-state Pauli polytope. Furthermore, we are able to distinguish unique features of the quantum mechanism exhibited by the subsystems, without having prior knowledge of their functionalities. For example, our previous work on the FMO complex showed that in the presence of quantum noise and a reaction center, the spectrum of 1-RDM occupations of the FMO system converges to the (0,0,0) point, which corresponds to the Slater determinant of the ground state [40]. It is clear from our present model that the system of interest in this paper converges to a classical ensemble instead due to the absence of the reaction center, showing the potential of the GPCs to be used for sensing the presence of an energy sink in similar light-harvesting complexes.

We can also observe two distinct types of 3-qubit interactions in the Pauli polytope. For example, Fig. 6 illustrates different helical behavior than noted in Figs. 5(a)–5(c). The set of physically accessible 1-RDMs is expanded to a greater extent when chromophores 7 and 8 constitute the third qubit in the system. Moreover, the rate at which the subsystems reach the classical ensemble state varies across the given examples (see Appendix C). These results demonstrate the temporal evolution of entanglement in five different multiqubit systems and illustrate how a single qubit can suppress or enhance the measured relaxation process. It is important to note that the present model is not limited to sensing by the FMO complex; rather it is an illustration of a theoretical framework that may be applied to an arbitrary multiqubit system exhibiting entanglement and that can be described using the GPC formalism in Eq. (3) and the Pauli polytope. We provide a scheme for designing a multiqubit sensor with the ability to act as a simplified quantum "computer" by receiving external stimuli, performing a sequence of calculations through gate

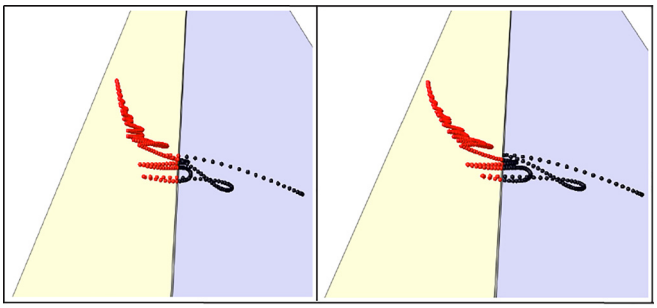

FIG. 6. Trajectories of different 3-qubit subsystems of the FMO complex for the first 2 ps of the energy transfer process. In each case, the time evolution produces an expanded set of 1-RDMs, violating the GPCs initially, and then converges to a classical ensemble at longer times. The two panels differ in the choice of 1 of the 3 qubits in the subsystem: (a) 127 and (b) 128. The 128 subsystem relaxes to its classical ensemble state at a faster rate than any of the other subsystems considered.

manipulation, and carrying an output to the measurement of the final state. In this paper, the FMO complex converts quantum information into quantum memory, which is then processed and measured using the GPC framework. Practically, this proof of concept could be implemented in the design of solid-state probes, where, for example, NV centers are functionalized with antenna complexes [72,73], which serve as mini quantum computers that may be used to distinguish environmental noise from the signal or to allow for initialization of the NV centers at different times.

Remarkably, not only do the GPCs behave as an indicator of entanglement in a multipartite system, but also they demonstrate that the essential features of such strong entanglement and correlation can be decoded from a knowledge of no more than the 1-RDM. Previous work has shown that GPCs of the 1-RDM contain important information about the many-fermion system and its wave function [41,44,74], and recently, it has been demonstrated that a combination of machine learning and RDMs may provide a significant reduction in the computational cost of calculating highly correlated systems [75]. Here we establish that the GPCs and the 1-RDM provide a general platform for constructing a multiqubit-driven class of quantum sensors that are capable of reporting on the environment by measuring and analyzing the openness of the quantum sensor.

III. CONCLUSIONS

Our results reveal that 3-qubit systems provide sufficient degrees of freedom for establishing an entanglement-enhanced interaction whose 1-RDM can discern between an open and a closed system. Therefore, we demonstrate how an entangled multiqubit sensor of low computational cost for simulation can be harnessed for performing nontrivial computations, acting as an effective few-qubit quantum "computer." The nonexponential measurement performed by the sensor uncovers whether the prepared state is interacting with the environment, in which case the pure-state Pauli polytope is violated. Here, the Pauli polytope is an important tool that visually highlights openness of the 3-qubit system as a function of time. The advantage of embedding multiqubit quantum systems in quantum sensors is that it enables more sophisticated state preparation and measurement schemes by exploiting fundamental restrictions of a pure-state quantum space, such as the GPCs and pure N-representability conditions, to enhance the sensitivity and fidelity of the quantum sensor to the environment. The computational complexity of checking the GPCs is determined by the cost of computing the eigenvalues (natural occupations) of the 1-RDM. The measurement and storage costs of the 1-RDM increase as N^2, while the computation of the 1-RDM's eigenvalues scales as N^3, where N is the number of qubits. Therefore, learning how to extract information on the system-environment interactions using single-qubit populations could lead to enhanced quantum sensors that maximally utilize quantum computational advantage.

Though the implementation of entangled multiqubit sensors would enable sensing beyond the standard limit, practical deployment of entanglement-enhanced quantum sensors, in part, relies on striking the correct balance between noise suppression and signal conservation. By acting on the border between quantum sensing and quantum computation, we present a scheme for the detection of environmental noise in a particular implementation of an entangled open quantum system by exploiting the Pauli polytope. Our open-system quantum sensing approach demonstrates how the constraints on fermionic correlation and entanglement can be used to extract enhanced sensing information on the noise-assisted relaxation process of a multiqubit system. We show how multiparticle entanglement in sensors of 3 and more qubits can be used to exploit the GPCs or, more generally, the pure-state N-representability conditions to sense the openness of the quantum system. Hence, the use of GPCs in quantum sensors offers an alternative paradigm for merging multiqubit quantum systems with quantum sensors.

ACKNOWLEDGMENTS

D.A.M. and G.S.E. gratefully acknowledge the U.S. National Science Foundation (NSF) QuBBE Quantum Leap Challenge Institute (NSF Grant No. OMA-2121044). D.A.M. further acknowledges NSF Grants No. CHE-2155082 and No. CHE-2035876 and the Department of Energy, Office of Basic Energy Sciences, Grant No. DE-SC0019215. I.A., L.M.S.-S., O.C.W., and J.S.H. acknowledge support from the NSF Graduate Research Fellowship Program, Grant No. DGE-1746045. J.S.H. further acknowledges support from a National Research Council postdoctoral fellowship.

APPENDIX A: CHEMICAL DYNAMICS

The time evolution of the eight-exciton density matrix is governed by the Lindblad equation [Eq. (7)], where D is the density matrix,

$$D = \sum_{k,l} \rho_l^k \, |\psi_k\rangle \, \langle\psi_l| \, ; \tag{A1}$$

ρ_l^k are the elements of D in the basis set of wave functions ψ_k, representing an excitation on the kth chromophore; and

$\hat{L}$ is the Lindblad operator, which accounts for interactions of the eight chromophores with the environment. The Lindblad operator is taken as a sum of three operators that describe dephasing, dissipation, and loss to the energy sink,

$$\hat{L}_{\text{deph}}(D) = \alpha \sum_k 2\,\langle k|\,D\,|k\rangle\,|k\rangle\,\langle k| - \{|k\rangle\,\langle k|\,, D\}, \quad \text{(A2)}$$

$$\hat{L}_{\text{diss}}(D) = \beta \sum_k 2\,\langle k|\,D\,|k\rangle\,|g\rangle\,\langle g| - \{|k\rangle\,\langle k|\,, D\}, \quad \text{(A3)}$$

$$\hat{L}_{\text{sink}}(D) = 2\gamma\,\langle 3|\,D\,|3\rangle\,|s\rangle\,\langle s| - \gamma\{|3\rangle\,\langle 3|\,, D\}. \quad \text{(A4)}$$

The $|g\rangle$ denotes the state in which each of the chromophores is in its ground state, the $|k\rangle$ represents each excited state having a single excitation on one of the chromophores, the $|s\rangle$ denotes the energy sink, and $|3\rangle$ indicates the excited state of the third chromophore multiplied by the ground states of the other seven chromophores.

The rate parameters in the Lindblad operators for dephasing (α), dissipation (β), and the sink (γ) are chosen to be 1.52×10^{-4} a.u. (33.4 cm^{-1}), 7.26×10^{-5} a.u. (15.9 cm^{-1}), and 1.21×10^{-8} a.u. (0.002 66 cm^{-1}), respectively, which is consistent with the definitions employed in Ref. [70]. In this model, dissipation transfers energy from the chromophores into the environment, and dephasing increases decoherence within the chromophore system. The "sink" captures the energy from the third chromophore that would be transferred to the reaction center. This feature was not present in the experimental setting; so this parameter is set to zero in the present model. Further analysis on the effect of dephasing on the presented results is described in Appendix E. The Lindbladian operators are Markovian in time, and the addition of non-Markovian terms is not expected to qualitatively change the results of this work. More details on the model used in this paper can be found in Refs. [76–78].

APPENDIX B: DERIVATION OF THE INITIAL DENSITY MATRIX FROM EXPERIMENTAL DATA

1. Construction of excitonic transition dipoles

To obtain realistic FMO site populations at the time of initialization, we calculated the 8×8 density matrix of the FMO complex right after coherent optical excitation of the ground state [Eq. (B1)], as seen in the ultrafast two-dimensional electronic spectroscopy experiments reported in the study by Higgins *et al.* [52]. The optical excitations correspond to the Q_y transition of each of the eight bacteriochlorophyll-a chromophores. The site transition dipole moments (TDMs) are therefore approximated to be the vectors joining two diagonal nitrogen atoms at the center of each of the chlorin moieties of the chromophores. The relevant nitrogen atom coordinates were obtained from the crystal structure of the FMO complex [79]. It is necessary to project these site TDMs in the exciton basis before incorporating the experimental conditions of Ref. [52], since time-domain spectroscopy resolves dynamics in excitonic energy levels, and not in the spatial sites. For this, we obtain the site-to-exciton unitary transformation matrix by diagonalizing the Hamiltonian in the site basis [Eq. (B2)] with energies expressed in cm^{-1} as in Ref. [68].

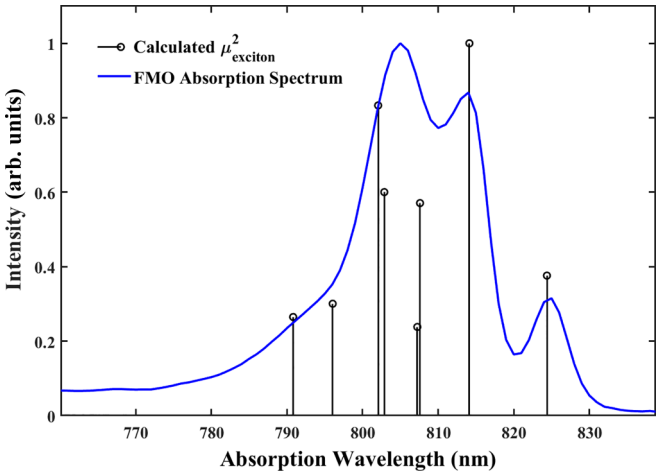

FIG. 7. The calculated excitonic transition dipole moment squared (black) is in good agreement with the linear absorption spectrum (blue).

2. Optical pulse interactions with excitonic transition dipole moments

An excited electronic population is created after the interaction with two optical pulses. In other words, the realistic qubits were initialized in the ultrafast spectroscopy experiment through the quantum system's interaction with two electromagnetic perturbations. We denote the ith excitonic state as $|e_i\rangle$, $i = 1, 2, \ldots, 8$. After exciting with two optical pulses, carrying energies of all eight excitonic transitions, the ground state population, $|g\rangle\langle g|$, can be excited into an ith excitonic population state, $|e_i\rangle\langle e_i|$, or into a coherence between the ith and jth states, $|e_i\rangle\langle e_j|$, considering all the unique double-sided Feynman pathways. Since each light-matter interaction entails a perturbation term of $-\mu \cdot E$, where E is the electric field of the perturbative radiation, the elements of the density matrix, ρ, can be written as

$$\rho_{ij} = \mu_i \mu_j E_i E_j \cos\theta_{ij}.$$

The perturbative electric field magnitudes at different energies E_i were obtained from the laser spectrum of the ultrafast spectroscopy experiment in Ref. [52]. θ_{ij} is the angle between

TABLE I. Qubit 1 populations over time in the specified chromophore subsystems.

Time (fs)	123	124	125	126	127	128
0	0.322	0.322	0.322	0.322	0.322	0.322
250	0.228	0.228	0.228	0.228	0.228	0.228
500	0.181	0.181	0.181	0.181	0.181	0.181
750	0.179	0.179	0.179	0.179	0.179	0.179
1000	0.163	0.163	0.163	0.163	0.163	0.163
1250	0.153	0.153	0.153	0.153	0.153	0.153
1500	0.149	0.149	0.149	0.149	0.149	0.149
1750	0.145	0.145	0.145	0.145	0.145	0.145
2000	0.142	0.142	0.142	0.142	0.142	0.142
3000	0.134	0.134	0.134	0.134	0.134	0.134
4000	0.130	0.130	0.130	0.130	0.130	0.130
5000	0.128	0.128	0.128	0.128	0.128	0.128
10000	0.124	0.124	0.124	0.124	0.124	0.124

the ith and jth TDM vectors. The term $\cos\theta_{ij}$ comes from the dipole orientational averaging that arises due to the TDMs being able to assume any configuration in three-dimensional space, since the experiments were conducted in the condensed phase [80]. μ_i^2 is plotted in Fig. 7 showing good agreement with the linear absorption spectrum of the Q_y excitonic transitions of the FMO complex. The initialized density matrix is thus

$$D = \begin{pmatrix} 0.091685 & 0.002176199 & 0.066362109 & 0.028780581 & -0.10200601 & 0.078137346 & -0.027569155 & -0.005531506 \\ & 0.322040254 & -0.174559029 & 0.101588016 & -0.111162506 & -0.031343411 & -0.032443933 & -0.01127451 \\ & & 0.144900733 & -0.037710647 & -0.017513904 & 0.066606204 & -0.002317347 & 0.001564286 \\ & & & 0.062229502 & -0.04568451 & 0.066426282 & -0.020214378 & -0.00182618 \\ & & & & 0.169527856 & -0.02623231 & 0.03989638 & 0.01313672 \\ & & & & & 0.196813726 & -0.024091979 & 0.004683091 \\ & & & & & & 0.011546785 & 0.002511428 \\ & & & & & & & 0.001255918 \end{pmatrix}, \tag{B1}$$

$$\hat{H}_{\text{site}} = \begin{pmatrix} 12461.0 & -87.0 & 4.2 & -5.2 & 5.5 & -14.0 & -6.1 & 21.0 \\ & 12486.0 & 28.0 & 6.9 & 1.5 & 8.7 & 4.5 & 4.2 \\ & & 12151.0 & -54.0 & -0.2 & -7.6 & 1.2 & 0.6 \\ & & & 12316.0 & -62.0 & -16.0 & -51.0 & -1.3 \\ & & & & 12458.0 & 60.0 & 1.7 & 3.3 \\ & & & & & 12614.0 & 29.0 & -7.9 \\ & & & & & & 12368.0 & -9.3 \\ & & & & & & & 12460.0 \end{pmatrix}. \tag{B2}$$

APPENDIX C: OCCUPATIONS OF THE EXCITED-STATE ORBITALS OVER TIME

The three smallest eigenvalues for each of the qubits in the considered 3-qubit subsystems over time are the populations of the excited-state orbitals during the relaxation process (Tables I–III). The columns in the tables denote different chromophore subsystems.

APPENDIX D: FENNA-MATTHEWS-OLSON COMPLEX POPULATION DYNAMICS

To obtain the exciton populations, the diagonal elements of the density matrix, D, are constructed from orthogonal transformation operators as follows:

$$p_i = V_i^T D_{\text{site}} V_i,$$

where p_i is the population of ith exciton and V_i is the ith eigenvector of the defined Hamiltonian, $\hat{H}$. The Fenna-Matthews-Olson (FMO) complex population dynamics, in the exciton basis, for the first 1 ps of the energy transfer process is shown in Fig. 8. Note that $\hat{H}$ and D_{site} are not diagonal in this case; therefore the initial conditions in Figs. 8 and 2 differ slightly.

TABLE II. Qubit 2 populations over time in the specified chromophore subsystems.

Time (fs)	123	124	125	126	127	128
0	0.145	0.092	0.170	0.197	0.092	0.092
250	0.158	0.158	0.158	0.158	0.158	0.158
500	0.175	0.175	0.175	0.175	0.175	0.175
750	0.163	0.163	0.163	0.163	0.163	0.163
1000	0.156	0.156	0.156	0.156	0.156	0.156
1250	0.153	0.153	0.153	0.153	0.153	0.153
1500	0.147	0.147	0.147	0.147	0.147	0.147
1750	0.144	0.144	0.144	0.144	0.144	0.144
2000	0.141	0.141	0.141	0.141	0.141	0.141
3000	0.134	0.134	0.134	0.134	0.134	0.134
4000	0.130	0.130	0.130	0.130	0.130	0.130
5000	0.127	0.127	0.127	0.127	0.127	0.127
10000	0.124	0.124	0.124	0.124	0.124	0.124

TABLE III. Qubit 3 populations over time in the specified chromophore subsystems.

Time (fs)	123	124	125	126	127	128
0	0.092	0.062	0.092	0.092	0.012	0.001
250	0.129	0.089	0.133	0.132	0.070	0.062
500	0.115	0.101	0.118	0.137	0.089	0.083
750	0.116	0.105	0.116	0.132	0.093	0.096
1000	0.114	0.108	0.115	0.126	0.104	0.114
1250	0.114	0.111	0.117	0.123	0.108	0.121
1500	0.114	0.113	0.117	0.122	0.111	0.125
1750	0.115	0.114	0.119	0.122	0.113	0.127
2000	0.115	0.116	0.119	0.122	0.115	0.128
3000	0.118	0.119	0.121	0.122	0.119	0.129
4000	0.120	0.121	0.123	0.123	0.121	0.128
5000	0.122	0.122	0.123	0.123	0.122	0.126
10000	0.124	0.124	0.124	0.124	0.124	0.124

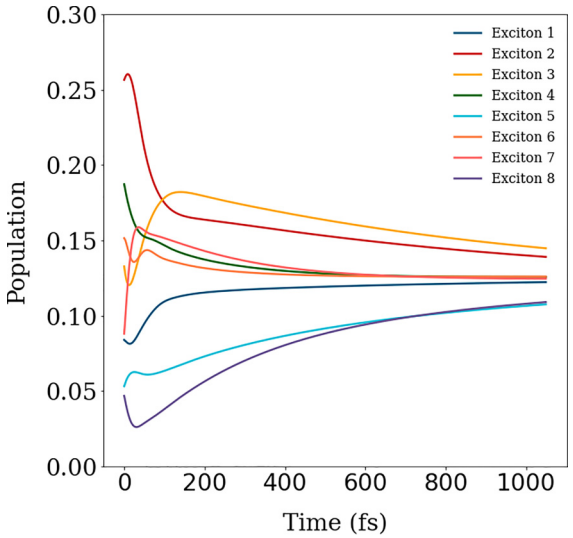

FIG. 8. Exciton populations of the FMO complex for the first 1 ps of the energy transfer process.

APPENDIX E: THE EFFECT OF DEPHASING ON THE PAULI POLYTOPE DYNAMICS

In Figs. 8 and 9, the dephasing parameter is increased to 100.2 cm^{-1}, which is three times greater than the parameter consistent with definitions in Ref. [70] used in the main text. This was done, first, to obtain a smooth exciton dynamics, since oscillations are dephasing driven, and second, to illustrate that our main conclusions hold even for the case of high dephasing. In Fig. 9, the time evolution produces an expanded set of 1-RDMs in each scenario, violating the GPCs initially, and then converges to the classical limit at longer times, as is the case with lower dephasing character. Varying only 1 qubit shows enhanced measurements of the relaxation processes of the remaining qubits in the system even in the presence of high dephasing, demonstrating the robustness of our qualitative conclusions to the choice of simulation parameters used in the main text.

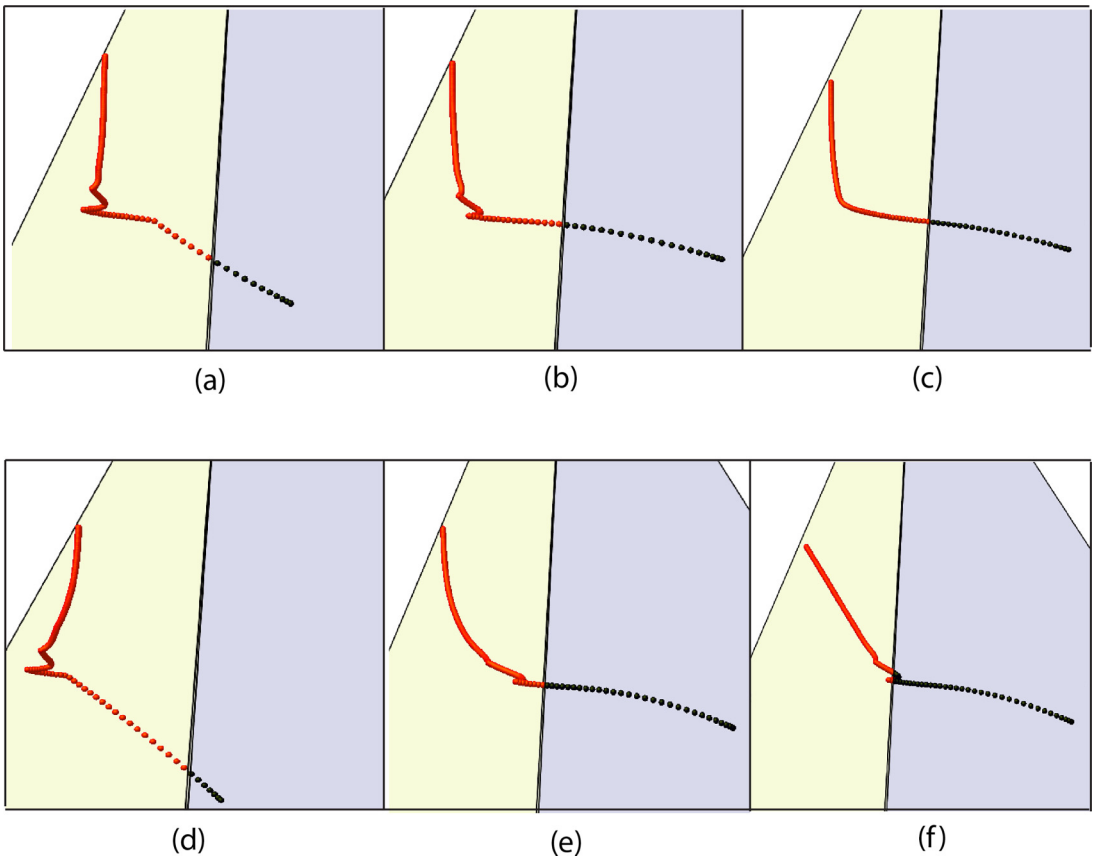

FIG. 9. Temporal trajectories of different 3-qubit subsystems of the FMO complex for the first 2 ps of the energy transfer process from the experimentally derived density matrix, with the dephasing parameter set to 100.2 cm^{-1}. The panels differ in the choice of 1 of the 3 qubits or chromophores in the subsystem: (a) 123, (b) 124, (c) 125, (d) 126, (e) 127, and (f) 128, where, for example, "123" denotes chromophores 1, 2, and 3.

[1] J. Grotti, S. Koller, S. Vogt, S. Häfner, U. Sterr, C. Lisdat, H. Denker, C. Voigt, L. Timmen, A. Rolland, F. N. Baynes, H. S. Margolis, M. Zampaolo, P. Thoumany, M. Pizzocaro, B. Rauf, F. Bregolin, A. Tampellini, P. Barbieri, M. Zucco *et al.*, Geodesy and metrology with a transportable optical clock, Nat. Phys. **14**, 437 (2018).

[2] A. D. Ludlow, M. M. Boyd, J. Ye, E. Peik, and P. O. Schmidt, Optical atomic clocks, Rev. Mod. Phys. **87**, 637 (2015).

[3] Z. Ahmed, Y. Alexeev, G. Apollinari, A. Arvanitaki, D. Awschalom, K. K. Berggren, K. Van Bibber, P. Bienias, G. Bodwin, M. Boshier, D. Bowring, D. Braga, K. Byrum, G. Cancelo, G. Carosi, T. Cecil, C. Chang, M. Checchin, S. Chekanov, A. Chou *et al.*, Quantum sensing for high energy physics, arXiv:1803.11306.

[4] C. L. Degen, F. Reinhard, and P. Cappellaro, Quantum sensing, Rev. Mod. Phys. **89**, 035002 (2017).

[5] M. Xie, X. Yu, L. V. H. Rodgers, D. Xu, I. Chi-Durán, A. Toros, N. Quack, N. P. de Leon, and P. C. Maurer, Biocompatible surface functionalization architecture for a diamond quantum sensor, Proc. Natl. Acad. Sci. USA **119**, e2114186119 (2022).

[6] R. Schirhagl, K. Chang, M. Loretz, and C. L. Degen, Nitrogen-vacancy centers in diamond: Nanoscale sensors for physics and biology, Annu. Rev. Phys. Chem. **65**, 83 (2014).

[7] J. F. Barry, J. M. Schloss, E. Bauch, M. J. Turner, C. A. Hart, L. M. Pham, and R. L. Walsworth, Sensitivity optimization for NV-diamond magnetometry, Rev. Mod. Phys. **92**, 015004 (2020).

[8] I. Lovchinsky, A. O. Sushkov, E. Urbach, N. P. De Leon, S. Choi, K. De Greve, R. Evans, R. Gertner, E. Bersin, C. Müller, L. Mcguinness, F. Jelezko, R. L. Walsworth, H. Park, and M. D. Lukin, Nuclear magnetic resonance detection and spectroscopy of single proteins using quantum logic, Science **351**, 836 (2016).

[9] M. H. Abobeih, J. Randall, C. E. Bradley, H. P. Bartling, M. A. Bakker, M. J. Degen, M. Markham, D. J. Twitchen, and T. H. Taminiau, Atomic-scale imaging of a 27-nuclear-spin cluster using a quantum sensor, Nature (London) **576**, 411 (2019).

[10] J. Walker, Optical absorption and luminescence in diamond, Rep. Prog. Phys. **42**, 1605 (1979).

[11] A. Gali, E. Janzén, P. Deák, G. Kresse, and E. Kaxiras, Theory of spin-conserving excitation of the $N{-}V^{-}$ center in diamond, Phys. Rev. Lett. **103**, 186404 (2009).

[12] G. Thiering and A. Gali, Theory of the optical spin-polarization loop of the nitrogen-vacancy center in diamond, Phys. Rev. B **98**, 085207 (2018).

[13] A. Gali, *Ab initio* theory of the nitrogen-vacancy center in diamond, Nanophotonics **8**, 1907 (2019).

[14] A. Mitra, H. Q. Pham, R. Pandharkar, M. R. Hermes, and L. Gagliardi, Excited states of crystalline point defects with multireference density matrix embedding theory, J. Phys. Chem. Lett. **12**, 11688 (2021).

[15] Y. Jin, M. Govoni, and G. Galli, Vibrationally resolved optical excitations of the nitrogen-vacancy center in diamond, npj Comput. Mater. **8**, 238 (2022).

[16] A. Alkauskas, B. B. Buckley, D. D. Awschalom, and C. G. Van de Walle, First-principles theory of the luminescence lineshape for the triplet transition in diamond NV centres, New J. Phys. **16**, 073026 (2014).

[17] G. Tóth and I. Apellaniz, Quantum metrology from a quantum information science perspective, J. Phys. A: Math. Theor. **47**, 424006 (2014).

[18] T.-X. Zheng, A. Li, J. Rosen, S. Zhou, M. Koppenhöfer, Z. Ma, F. T. Chong, A. A. Clerk, L. Jiang, and P. C. Maurer, Preparation of metrological states in dipolar-interacting spin systems, npj Quantum Inf. **8**, 150 (2022).

[19] C. M. Caves, Quantum-mechanical noise in an interferometer, Phys. Rev. D **23**, 1693 (1981).

[20] D. J. Wineland, J. J. Bollinger, W. M. Itano, F. L. Moore, and D. J. Heinzen, Spin squeezing and reduced quantum noise in spectroscopy, Phys. Rev. A **46**, R6797(R) (1992).

[21] M. Kitagawa and M. Ueda, Squeezed spin states, Phys. Rev. A **47**, 5138 (1993).

[22] O. Hosten, N. J. Engelsen, R. Krishnakumar, and M. A. Kasevich, Measurement noise 100 times lower than the quantum-projection limit using entangled atoms, Nature (London) **529**, 505 (2016).

[23] O. Hosten, R. Krishnakumar, N. J. Engelsen, and M. A. Kasevich, Quantum phase magnification, Science **352**, 1552 (2016).

[24] V. Giovannetti, S. Lloyd, and L. Maccone, Advances in quantum metrology, Nat. Photon. **5**, 222 (2011).

[25] L. Pezzè, Entanglement-enhanced sensor networks, Nat. Photonics **15**, 74 (2021).

[26] Z. Zhang, S. Mouradian, F. N. C. Wong, and J. H. Shapiro, Entanglement-enhanced sensing in a lossy and noisy environment, Phys. Rev. Lett. **114**, 110506 (2015).

[27] S. Colombo, E. Pedrozo-Peñafiel, and V. Vuletić, Entanglement-enhanced optical atomic clocks, Appl. Phys. Lett. **121**, 210502 (2022).

[28] S. Zaiser, T. Rendler, I. Jakobi, T. Wolf, S.-Y. Lee, S. Wagner, V. Bergholm, T. Schulte-Herbrüggen, P. Neumann, and J. Wrachtrup, Enhancing quantum sensing sensitivity by a quantum memory, Nat. Commun. **7**, 12279 (2016).

[29] R. A. Thomas, M. Parniak, C. Østfeldt, C. B. Møller, C. Bærentsen, Y. Tsaturyan, A. Schliesser, J. Appel, E. Zeuthen, and E. S. Polzik, Entanglement between distant macroscopic mechanical and spin systems, Nat. Phys. **17**, 228 (2021).

[30] A. Szabo and N. S. Ostlund, *Modern Quantum Chemistry: Introduction to Advanced Electronic Structure Theory*, 1st ed. (Dover, Mineola, NY, 1996).

[31] H. M. Wiseman and J. A. Vaccaro, Entanglement of indistinguishable particles shared between two parties, Phys. Rev. Lett. **91**, 097902 (2003).

[32] W. Pauli, Über den Zusammenhang des Abschlusses der Elektronengruppen im Atom mit der Komplexstruktur der Spektren, Z. Phys. **31**, 765 (1925).

[33] M. Walter, B. Doran, D. Gross, and M. Christandl, Entanglement polytopes: Multiparticle entanglement from single-particle information, Science **340**, 1205 (2013).

[34] S. E. Smart and D. A. Mazziotti, Quantum-classical hybrid algorithm using an error-mitigating N-representability condition to compute the Mott metal-insulator transition, Phys. Rev. A **100**, 022517 (2019).

[35] D. Gibney, J.-N. Boyn, and D. A. Mazziotti, Toward a resolution of the static correlation problem in density functional theory from semidefinite programming, J. Phys. Chem. Lett. **12**, 385 (2021).

[36] J.-N. Boyn and D. A. Mazziotti, Sparse non-orthogonal wave function expansions from the extension of the generalized Pauli constraints to the two-electron reduced density matrix, J. Chem. Phys. **150**, 144102 (2019).

[37] C. Schilling, M. Altunbulak, S. Knecht, A. Lopes, J. D. Whitfield, M. Christandl, D. Gross, and M. Reiher, Generalized Pauli constraints in small atoms, Phys. Rev. A **97**, 052503 (2018).

[38] C. L. Benavides-Riveros and C. Schilling, Natural extension of Hartree–Fock through extremal 1-fermion information: Overview and application to the lithium atom, Z. Phys. Chem. **230**, 703 (2016).

[39] R. Chakraborty and D. A. Mazziotti, Sufficient condition for the openness of a many-electron quantum system from the violation of a generalized Pauli exclusion principle, Phys. Rev. A **91**, 010101(R) (2015).

[40] R. Chakraborty and D. A. Mazziotti, Noise-assisted energy transfer from the dilation of the set of one-electron reduced density matrices, J. Chem. Phys. **146**, 184101 (2017).

[41] C. Schilling, D. Gross, and M. Christandl, Pinning of fermionic occupation numbers, Phys. Rev. Lett. **110**, 040404 (2013).

[42] C. Schilling, Quasipinning and its relevance for N-fermion quantum states, Phys. Rev. A **91**, 022105 (2015).

[43] C. Schilling, Hubbard model: Pinning of occupation numbers and role of symmetries, Phys. Rev. B **92**, 155149 (2015).

[44] R. Chakraborty and D. A. Mazziotti, Generalized Pauli conditions on the spectra of one-electron reduced density matrices of atoms and molecules, Phys. Rev. A **89**, 042505 (2014).

[45] R. Chakraborty and D. A. Mazziotti, Sparsity of the wavefunction from the generalized Pauli exclusion principle, J. Chem. Phys. **148**, 054106 (2018).

[46] S. E. Smart, D. I. Schuster, and D. A. Mazziotti, Experimental data from a quantum computer verifies the generalized Pauli exclusion principle, Comm. Phys. **2**, 11 (2019).

[47] L. M. Sager, S. E. Smart, and D. A. Mazziotti, Preparation of an exciton condensate of photons on a 53-qubit quantum computer, Phys. Rev. Res. **2**, 043205 (2020).

[48] R. E. Borland and K. Dennis, The conditions on the one-matrix for three-body fermion wavefunctions with one-rank equal to six, J. Phys. B: At. Mol. Phys. **5**, 7 (1972).

[49] A. Higuchi, A. Sudbery, and J. Szulc, One-qubit reduced states of a pure many-qubit state: Polygon inequalities, Phys. Rev. Lett. **90**, 107902 (2003).

[50] A. A. Klyachko, Quantum marginal problem and N-representability, J. Phys.: Conf. Ser. **36**, 72 (2006).

[51] R. E. Fenna and B. W. Matthews, Chlorophyll arrangement in a bacteriochlorophyll protein from *Chlorohium limicola*, Nature (London) **258**, 573 (1975).

[52] J. S. Higgins, L. T. Lloyd, S. H. Sohail, M. A. Allodi, J. P. Otto, R. G. Saer, R. E. Wood, S. C. Massey, P.-C. Ting, R. E. Blankenship, and G. S. Engel, Photosynthesis tunes quantum-mechanical mixing of electronic and vibrational states to steer exciton energy transfer, Proc. Natl. Acad. Sci. USA **118**, e2018240118 (2021).

[53] A. J. Coleman, Structure of fermion density matrices, Rev. Mod. Phys. **35**, 668 (1963).

[54] D. M. Greenberger, GHZ (Greenberger–Horne–Zeilinger) theorem and GHZ states, in *Compendium of Quantum Physics*, edited by D. Greenberger, K. Hentschel, and F. Weinert (Springer, Berlin, 2009), pp. 258–263.

[55] W. Dür, G. Vidal, and J. I. Cirac, Three qubits can be entangled in two inequivalent ways, Phys. Rev. A **62**, 062314 (2000).

[56] R. E. Blankenship, Molecular mechanisms of photosynthesis, Q. Rev. Biol. **78**, 234 (2003).

[57] G. S. Engel, T. R. Calhoun, E. L. Read, T.-K. Ahn, T. Mančal, Y.-C. Cheng, R. E. Blankenship, and G. R. Fleming, Evidence for wavelike energy transfer through quantum coherence in photosynthetic systems, Nature (London) **446**, 782 (2007).

[58] H. Lee, Y.-C. Cheng, and G. R. Fleming, Coherence dynamics in photosynthesis: Protein protection of excitonic coherence, Science **316**, 1462 (2007).

[59] M. Mohseni, P. Rebentrost, S. Lloyd, and A. Aspuru-Guzik, Environment-assisted quantum walks in photosynthetic energy transfer, J. Chem. Phys. **129**, 174106 (2008).

[60] D. M. Wilkins and N. S. Dattani, Why quantum coherence is not important in the Fenna–Matthews–Olsen complex, J. Chem. Theory Comput. **11**, 3411 (2015).

[61] J. S. Higgins, M. A. Allodi, L. T. Lloyd, J. P. Otto, S. H. Sohail, R. G. Saer, R. E. Wood, S. C. Massey, P.-C. Ting, R. E. Blankenship, and G. S. Engel, Redox conditions correlated with vibronic coupling modulate quantum beats in photosynthetic pigment–protein complexes, Proc. Natl. Acad. Sci. USA **118**, e2112817118 (2021).

[62] M. Maiuri, E. E. Ostroumov, R. G. Saer, R. E. Blankenship, and G. D. Scholes, Coherent wavepackets in the Fenna–Matthews–Olson complex are robust to excitonic-structure perturbations caused by mutagenesis, Nat. Chem. **10**, 177 (2018).

[63] F. Häse, C. Kreisbeck, and A. Aspuru-Guzik, Machine learning for quantum dynamics: Deep learning of excitation energy transfer properties, Chem. Sci. **8**, 8419 (2017).

[64] Z. Hu, K. Head-Marsden, D. A. Mazziotti, P. Narang, and S. Kais, A general quantum algorithm for open quantum dynamics demonstrated with the Fenna-Matthews-Olson complex, Quantum **6**, 726 (2022).

[65] M. Chávez-Huerta and F. Rojas, Environment-assisted quantum discord in the chromophores network of light-harvesting complexes, Quantum Inf. Process. **21**, 347 (2022).

[66] F. Gallina, M. Bruschi, and B. Fresch, Strategies to simulate dephasing-assisted quantum transport on digital quantum computers, New J. Phys. **24**, 023039 (2022).

[67] A. Ullah and P. O. Dral, Predicting the future of excitation energy transfer in light-harvesting complex with artificial intelligence-based quantum dynamics, Nat. Commun. **13**, 1930 (2022).

[68] A. Kell, R. E. Blankenship, and R. Jankowiak, Effect of spectral density shapes on the excitonic structure and dynamics of the Fenna–Matthews–Olson trimer from *Chlorobaculum tepidum*, J. Phys. Chem. A **120**, 6146 (2016).

[69] H. P. Breuer and F. Petruccione, *The Theory of Open Quantum Systems* (Oxford University Press, Oxford, 2002).

[70] M. B. Plenio and S. F. Huelga, Dephasing-assisted transport: Quantum networks and biomolecules, New J. Phys. **10**, 113019 (2008).

[71] Z. Hu, R. Xia, and S. Kais, A quantum algorithm for evolving open quantum dynamics on quantum computing devices, Sci. Rep. **10**, 3301 (2020).

[72] J. Tisler, R. Reuter, A. Lämmle, F. Jelezko, G. Balasubramanian, P. R. Hemmer, F. Reinhard, and J. Wrachtrup, Highly efficient Fret from a single nitrogen-vacancy

center in nanodiamonds to a single organic molecule, ACS Nano. **5**, 7893 (2011).

[73] S. Pezzagna and J. Meijer, Quantum computer based on color centers in diamond, Appl. Phys. Rev. **8**, 011308 (2021).

[74] C. L. Benavides-Riveros, J. M. Gracia-Bondía, and M. Springborg, Quasipinning and entanglement in the lithium isoelectronic series, Phys. Rev. A **88**, 022508 (2013).

[75] L. M. Sager-Smith and D. A. Mazziotti, Reducing the quantum many-electron problem to two electrons with machine learning, J. Am. Chem. Soc. **144**, 18959 (2022).

[76] D. A. Mazziotti, Effect of strong electron correlation on the efficiency of photosynthetic light harvesting, J. Chem. Phys. **137**, 074117 (2012).

[77] R. Chakraborty and D. A. Mazziotti, Structure of the one-electron reduced density matrix from the generalized Pauli exclusion principle, Int. J. Quantum Chem. **115**, 1305 (2015).

[78] N. Skochdopole and D. A. Mazziotti, Functional subsystems and quantum redundancy in photosynthetic light harvesting, J. Phys. Chem. Lett. **2**, 2989 (2011).

[79] D. E. Tronrud, J. Wen, L. Gay, and R. E. Blankenship, The structural basis for the difference in absorbance spectra for the FMO antenna protein from various green sulfur bacteria, Photosynthesis Res. **100**, 79 (2009).

[80] P. Hamm and M. Zanni, *Concepts and Methods of 2D Infrared Spectroscopy* (Cambridge University Press, Cambridge, 2011).